ICEF2023-110189

COMBUSTION RESEARCH IN WIDE DCN RANGE SYNTHETIC AVIATION FUELS IN A HIGH COMPRESSION RATIO ENGINE

Dr. Valentin Soloiu Georgia Southern University Statesboro, GA

Amanda Weaver Georgia Southern University Statesboro, GA

James Willis Georgia Southern University Statesboro, GA

Aidan Rowell Georgia Southern University Statesboro, GA

Nicholas Dillon Georgia Southern University Statesboro, GA

ABSTRACT

An investigation was conducted on the performance and emissions characteristics of two Fischer-Tropsch (F-T) synthetic kerosenes, Gas-to-Liquid (GTL) S8 and Coal-to-Liquid (CTL) Iso-Paraffinic Kerosene (IPK), in a high compression ratio research engine with separate combustion chamber and using neat ULSD as a baseline. A 50% and a 70% by mass blend S8 with ULSD and a 50% and a 70% by mass blend of IPK with ULSD were analyzed for performance and emissions at 5, 6, and 7 bar Indicated Mean Effective Pressure (IMEP) and 2400 rpm.

Additionally, neat S8, neat IPK, and neat ULSD were investigated in the Constant Volume Combustion Chamber (CVCC) for Ignition Delay (ID), Combustion Delay (CD), and Derived Cetane Number (DCN). S8 was found to have the highest DCN at 62 with very short ID and CD while IPK was found to have the lowest DCN at 26 and with the longest ID and CD. ULSD has a DCN between the two F-T fuels at 48. As a result of its long ID and CD, IPK showed extended regions of Low Temperature Heat Release (LTHR) and Negative Temperature Coefficient Region (NTCR) in the CVCC. It was also found that neat IPK, 50ULSD50IPK, and 30ULSD70IPK exhibit little to no ringing events at peak pressure and after High Temperature Heat Release (HTHR).

In the research engine, peak heat release for ULSD, 50ULSD50S8, and 50ULSD50IPK was found to be 24.2 J/CAD, 20.5 J/CAD, and 23.4 J/CAD respectively. Due to the increase of the DCN with the addition of S8 to the blend, the 50ULSD50S8 blend exhibited minimal difference between the pre-chamber and the main chamber as it ignites earlier in the cycle with the flame front traveling quickly to the main chamber. IPK, however, had a short physical ignition delay and a long chemical ignition delay, as indicated by its low DCN, takes longer to ignite and creates a more homogeneous mixture in the highly turbulent pre-chamber. This causes a spike in heat release in the pre-chamber before the flame front propagates to the main chamber. This resulted in 50ULSD50IPK having the highest Peak Pressure Rise Rate (PPRR) and 50ULSD50S8 having the lowest PPRR. While both fuel blends reduced the soot emissions due to their low aromatic content, 50ULSD50IPK showed a 25% reduction in soot when compared to ULSD while 50ULSD50S8 showed only a 6% reduction in soot when compared to neat ULSD. There was a increase in CO emissions with the addition of IPK and a reduction in CO at low load with the addition of S8. With both F-T fuels, CO₂ and NO_x were found to decrease.

Keywords: GTL, CTL, DCN, ID, CD, IDI, Fischer-Tropsch

NOMENCLATURE

Α Area

AFR Air Fuel Ratio

AHRR Apparent Heat Release

ATDC After Top Dead Center

BTDC Before Top Dead Center

BMEP Break Mean Effective Pressure

CAD Crank Angle Degree

Crank Angle Degree @ 10% mass burned CA10

Crank Angle Degree @ 50% mass burned CA50

Crank Angle Degree @ 90% mass burned CA90

Combustion Delay CD

CDC Conventional Diesel Combustion

Compression Ignition CI CO Carbon Monoxide

 CO_2 Carbon Dioxide Constant

CVCC Constant Volume Combustion Chamber

D Engine Bore

Ct

DCN Derived Cetane Number

Dv10 Largest Droplet Size of 10% of Fuel Spray
 Dv50 Largest Droplet Size of 50% of Fuel Spray
 Dv90 Largest Droplet Size of 90% of Fuel Spray

DTA Differential Thermal Analysis

F-T Fischer-Tropsch

FTIR Fourier Transform Spectroscopy

HHV Higher Heating Value

HTHR High Temperature Heat Release

ID Ignition DelayIDI Indirect InjectionIPK Iso-Paraffinic Kerosene

IMEP Indicated Mean Effective Pressure

LHV Lower Heating Value

LTHR Low Temperature Heat Release

N Engine Speed

NTCR Negative Temperature Coefficient Region

 $egin{array}{ll} NOx & Nitrogen oxides \\
ho(lpha) & In-cylinder gas density \\ PPRR & Peak Pressure Rise Rate \\ Re & Reynolds Number \\ RPM & Revolutions Per Minute \\ \end{array}$

S Stroke

SMD Sauter Mean Diameter

TA10 Temperature @ 10% mass vaporized TA50 Temperature @ 10% mass vaporized TA90 Temperature @ 90% mass vaporized

TGA Thermogravimetric Analysis

 T_W Wall Temperature $\lambda(\alpha)$ Thermal Conductivity $\mu(\alpha)$ Viscosity In-cylinder Gases ULSD Ultra-Low Sulfur Diesel

INTRODUCTION

With the rising global concern for the availability of fossil fuels and the increasing demand for alternative fuel sources, research into synthetic fuels and the effect of changing fuel properties has never been more important [1]. Internal combustion engines are a long-standing technology that is well understood and has been the backbone of power generation for over a century. With the increasing concerns for not only the atmospheric impact of fossil fuel combustion, but also the expansion of the aerospace field, there is a demand for alternative fuel sources.

There are a wide range of processes and feedstocks which can be used to produced hydrocarbon fuels for internal combustion engines which vary in both combustion properties and thermophysical properties. One such process which shows promise in the development of synthetic fuels from both biomass feedstocks as well as coal and natural gas is Fischer-Tropsch Synthesis [2]. This process is used to create purer, clean burning alternative fuels which have been shown in previous research to reduce emissions and increase efficiency in internal combustion engines [3-5].

The source of the feedstock, however, results in changes in the chemical composition of the resulting fuel which have a significant impact on the combustion, fluidic, and thermophysical properties of the resulting fuel. For compression ignition engines, one of the primary factors which determines the performance of a fuel is the Derived Cetane Number (DCN) indicating the fuel's affinity for autoignition [6,7].

Chemical composition has a strong relationship with the DCN, ID, and CD of the fuel. It has been shown in previous research that the increase in the wt% of straight chain hydrocarbons contributes to a higher ignition delay while an increase in the abundance of double bonded cyclo-paraffins and iso-paraffins increases the ID as the chemical structure is more stable [8,9]. Initial investigations were performed on neat IPK and a 50/50 mass blend of IPK with ULSD in the same IDI engine platform by Soloiu et. al. [10]. It was found that although IPK exhibits a long period of combustion and minimal ringing in the CVCC, it produced significant ringing intensity and detonation caused by the combination of autoignition resistance and rapid mixture formation. These characteristics were identified as the chemical and physical ignition delays of the researched fuels.

In this study, an investigation was conducted on the thermophysical properties, fundamental combustion characteristics, and the performance and emissions produced when run through an experimental Indirect Injection (IDI) Compression Ignition (CI) engine. The research engine was chosen for its highly turbulent separate combustion chamber and high compression ratio.

THERMOPHYSICAL PROPERTIES

A variety of investigative procedures were performed in the authors' labs, to determine the thermophysical properties of neat ULSD, IPK, and S8. These procedures help to further analyze the fuels' combustion characteristics in the CI engine and the CVCC and present a trend that can help explain results. For each fuel, the spray droplet distribution, spray pattern, and mixture formation were analyzed. Additionally, the vaporization rate and low temperature oxidation for each fuel was determined using thermogravimetric analysis and differential thermal analysis. These properties were investigated due to their effect on the ignition delay of the fuel. Additional investigations were performed to determine the fuel's heat of combustion, viscosity, and volatility. The heat of combustion was determined with a Parr 1341 digital constant volume calorimeter. The viscosity was determined using a Brookfield DV-II +Pro rotational viscometer.

Evaluated in the investigations of the thermophysical properties are the chemical and physical ignition delays for ULSD, IPK, and S8. The physical ignition delay is the time from Start of Injection (SOI) to the point at which the main exothermic reactions begin to take place [11]. This delay is affected by fuel properties such as volatility, viscosity, density, and other physical properties of the fuel. The chemical ignition delay begins where the physical ignition delay period ends, where the main exothermic reactions take place, and lasts until the Start of Combustion (SOC). The point where the physical and chemical ignition delays separate is referred to as the Point of Inflection (POI) [12]. The chemical ignition delay depends on the chemical

composition of the fuel and refers to the time it takes for the fuel to complete pre-flame reactions.

Comparing the thermophysical properties of ULSD to both IPK and S8, it is apparent that the F-T fuels are more favorable for combustion, because its lower thermophysical properties would reduce the physical ignition delay [13-16].

Some of the critical thermophysical properties such as Ignition Delay (ID), Combustion Delay (CD), Derived Cetane Number (DCN), Lower Heating Value (LHV), and Higher Heating Value (HHV) are provided below in Table 1. The chemical composition of each fuel including the paraffin and hydrocarbon distributions are provided in Table 2.

Table 1: Thermophysical Properties of Neat Researched Fuels / % Difference from USLD

	*** **		
	ULSD	IPK POSF7629	S8 POSF5109
LHV (MJ/kg)	41.1	44.25/ +7.66	42.04/ +2.29
DCN	48.56	25.88/ -46.71	62/ +27.68
Avg. ID (ms)	3.46	5.3/+53.18	2.74/ -20.81
Avg. CD (ms)	4.95	17.2/ +247.47	3.9/ -21.21
Viscosity @ 40°C (cP)	2.44	1.02/ -58.20	1.3/ -46.72
SMD [µm]	22.36	14.96/ -33.09	18.83/ -15.79
Density @ 26°C (kg/m³)	850	740/ -12.94	755/ -11.18

^{*}All values were measured using In-House Instruments from Georgia Southern's Automotive Combustion Laboratory

Table 2: Chemical Composition of Neat Researched Fuels [16,17] / % Difference from USLD

[16,17]7 % Difference from OSLD			
Composition	ULSD	Sasol IPK	Shell GTL(S8)
n-Paraffins (wt%)	16.4	2.1/ -87.20	17.7/ 7.93
Iso-paraffins (wt%)	18.4	88/ +378.26	82/+345.65
Cyclo-paraffins (wt%)	35	9/ -74.29	<0.4/ -98.86
Aromatics (wt%)	30	<0.5/ -98.33	<0.1/ -99.67
Total sulfur (wt%)	<15	<0.001/-99.99	<0.001/ -99.99

Thermal Stability and Low-Temperature Oxidation

Continuing investigations into the thermophysical properties and chemical compositions of ULSD, IPK, and S8, another analysis was conducted to determine the combustion properties of these fuels. The oxidation of these fuels at low temperatures was investigated using thermogravimetric analysis (TGA), and the thermal stability was examined using differential thermal analysis (DTA). These analyses were conducted using the Shimadzu DTG-60 and was conducted using a small sample of each research fuel weighing approximately 10 mg. The DTG-60's furnace was heated from 20°C to 600°C in 20°C increments per minute. A constant air flow rate of 15mL/min was flushed

through the furnace to continuously purge the furnace of oxidative gases. To ensure that the results were accurate, inert alumina powder was used as a baseline material in tandem with each research fuel, which the fuel would be compared to as the analysis was conducted as it has negligible loss in mass at all operating temperatures.

The TGA is used to measure the vaporization rate of the research fuel with respect to the percent reduction in the mass as a function of temperature. Based on the TGA data shown in Figure 1, both IPK and S8 are shown to have a significantly greater rate of vaporization than that of ULSD, with IPK having the greatest rate of vaporization. The high rate of vaporization in IPK and S8 (particularly in IPK) indicates that these fuels are much more volatile than ULSD, again with IPK displaying the greatest volatility.

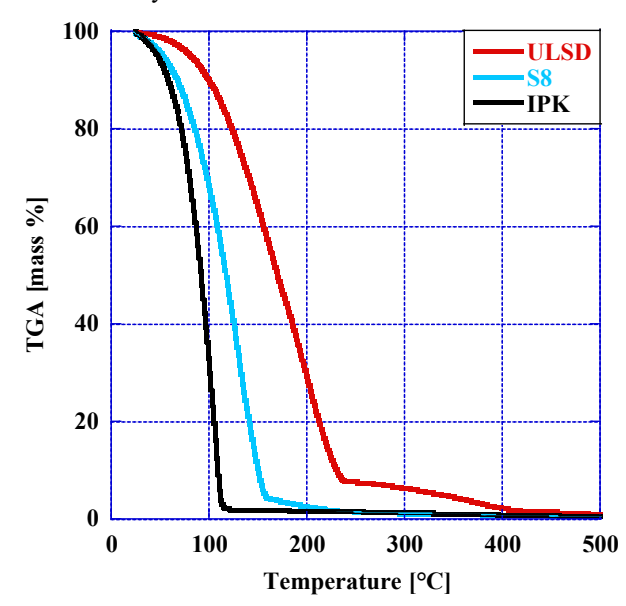


Figure 1: Thermogravimetric Analysis of the Neat Researched Fuels in Sample Mass Percent of the Fuel

The TGA data of ULSD, IPK, and S8 can be examined even further in Table 3, where the values shown are the temperatures at which 10%, 50%, and 90% of the research fuel's initial mass is vaporized. These points are denoted as TA(10), TA(50), and TA(90) respectively. IPK was found to have the highest volatility with a TA(90) value comparable to ULSD's TA(10) value at 108.71°C and 100°C respectively. S8 fell between the two with a TA(90) value comparable to ULSD's TA(50) value at 15.04°C and 170°C respectively.

Table 3: Thermogravimetric Analysis (TGA)

	ULSD	IPK	S8
TA (10) °C	100.0	58.2	67.2
TA (50) °C	170.0	91.4	117.1
TA (90) °C	230.3	108.71	150.04

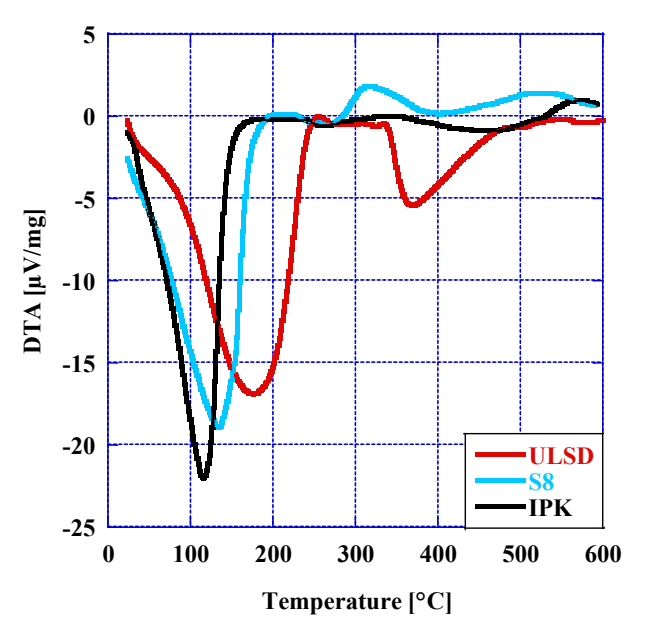


Figure 2: Differential Thermal Analysis of the Neat Researched Fuels

The results of the DTA show that at low temperatures, both IPK and S8 have a much higher rate of energy release and absorption than ULSD with the graph shown in Figure 2. At this temperature range, IPK and S8 are comparable, though IPK achieves a greater energy release and absorption rate and at a slightly lower temperature than S8. At mid-range temperatures (150°C ~ 350°C), IPK remains mostly stable, indicating a lack of energy absorption or release processes. At higher temperatures (350°C+), IPK undergoes a slight dip and then an exothermic process until reaching a positive peak just before 600°C. ULSD during the same mid-range temperatures is much less stable than IPK, displaying a drastic exothermic process following its negative peak just after 150°C, a brief plateau, and a significant endothermic process before 350°C.

At higher temperatures, ULSD undergoes a prolonged exothermic process before stabilizing and remaining stable at around 450°C. Lastly, S8 at mid-range temperatures is comparable to IPK until around 270°C, where the fuel undergoes an exothermic process, reaches its positive peak, then begins to decrease. At higher temperatures, S8 remains unstable, undergoing significant endothermic and exothermic processes until 600°C. Thus, the fuels can be organized in order of overall stability, from most stable to least stable at medium temperatures: IPK, S8, ULSD. The differences in the DTA between IPK and ULSD can be attributed to the more prevalent and heavier hydrocarbons present in ULSD, as well as the higher volatility of IPK. IPK and S8 are composed primarily of unsaturated branch iso-paraffins, which also contribute to the increased rates of energy release and absorption.

Spray Atomization, Mixture Formation, and Droplet Distribution using Mie Scattering He-Ne Laser Analysis

An analysis was conducted on the spray atomization, droplet distribution, and mixture formation of each of the

researched fuels using a Malvern Spraytec He-Ne laser. This apparatus is shown in Figure 3. Fuels were injected 100mm away from the laser beam at a pressure of 180 bar. Data was taken from 28 light detectors at a rate of 10kHz and recorded from 0.1 ms before the trigger to 5 ms after the trigger. The recorded data is then interpreted using Mie Scattering and Fraunhofer diffraction theory to determine the Sauter Mean Diameter (SMD) of the spray droplets due to the diffraction of the laser.

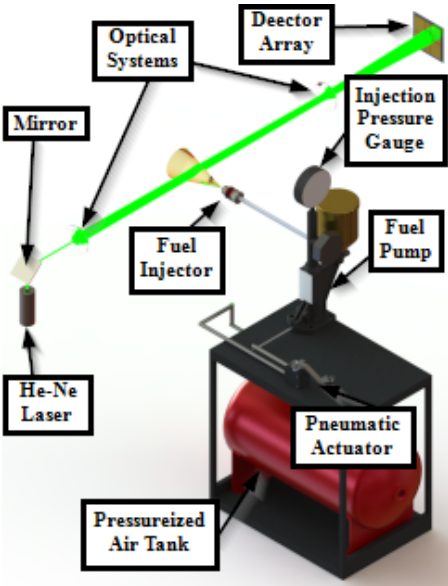


Figure 3: Malvern Mie Scattering He-Ne Laser Spraytech Apparatus

The SMD is determined with two equations which describe the scattering of unpolarized light by a spherical droplet. (Equation 1) [19].

$$I(\theta) = \frac{I_0}{2k^2a^2}([S_1(\theta)]^2 + [S_2(\theta)]^2)$$
 (1)

In Equation 1, $I(\theta)$ represents the light intensity after being scattered as a function of the angle θ , the angle at which the light hits the droplet relative to where it was detected. $S_1(\theta)$ and $S_2(\theta)$ represent complex, dimensionless functions which account for the change in amplitude of the parallel and perpendicular polarized light. Additionally, a is the measured distance between the light detectors and the light source, k is the wave number in $2\pi/\lambda$, and I_0 describes the initial intensity of the beam [19].

Because the above equation is for ideal spherical droplets, and spray droplets in practically are rarely perfectly spherical, a more practical application can be found in the Fraunhofer diffraction theory. This theory is well suited because it does not rely on the optical properties of the droplet and can be used in cases where the droplet is in a variety of mixtures and shapes. The terminology for the equation is the same as above, with the addition of the dimensionless size parameter $\alpha=\pi x/\lambda$, where x is the particle size.

$$I(\theta) = \frac{I_0}{2k^2a^2}\alpha^4 \left(\frac{J_1(\alpha\sin(\theta))}{\alpha\sin\sin(\theta)}\right)$$
 (2)

The averages for both SMD and droplet distribution were taken from each of the three research fuels in order to provide an accurate representation of the spray profile of the fuels. These results are presented in Figure 4. The lowest droplet size over the control volume in the spray belonged to IPK, followed by S8, then ULSD with the largest overall droplet size. This is due to the fact that IPK has the lowest viscosity of the three fuels, allowing it to atomize much easier, and resulting in a smaller droplet diameter. In terms of droplet diameter distribution, S8 and ULSD are much more comparable and similar in shape, although S8 is shown to have a slightly smaller droplet distribution.

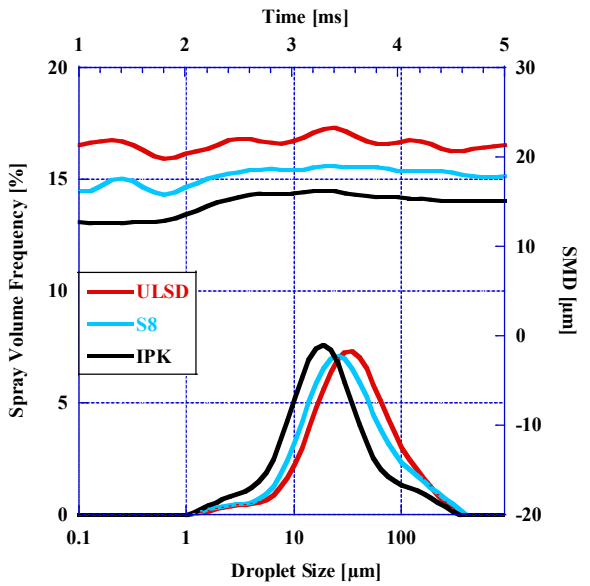


Figure 4: Spray Development and Droplet Frequency for Each of the Neat Researched Fuels

This is reflected as well in the Ohnesorge number of each fuel representing the droplets of fuel to either stay together or split apart by relating the internal viscous forces with external surface tension [20-22].

The Ohnesorge number was calculated using Equation 3, for each of the neat, researched fuels using both values found in literature in addition to those gathered using in-house equipment. The results of this analysis are shown in Table 4.

$$Oh = \frac{\mu}{\sqrt{\rho * \sigma * l_c}} \tag{3}$$

Table 4: Values for Internal Viscosity Dissipation and Surface Tension Energy for Neat Researched Fuels

Research Fuel	Surface Tension* [N/m]	Viscosity [cP]	SMD [µm]	Density [g/cm³]	Oh
ULSD	28.02	2.44	22.36	0.850	0.1057
S8	22.30	1.30	18.83	0.755	0.0680
IPK	20.30	1.02	14.96	0.740	0.0730

*Value found from Literature [21,22]

The results of Ohnesorge numbers obtained, align well and in direct relation with the values of surface tension, viscosity, and SMD and the density of the fuels.

Constant Volume Combustion Chamber (CVCC) Analysis of Fundamental Combustion

For the CVCC experimentation, a Petroleum Analysis Company (PAC) CID 510 was used to determine the Ignition Delay (ID), Combustion Delay (CD), and the Derived Cetane Number (DCN) of the researched fuels. A schematic of the external geometry and a cross section of the internal geometry of the combustion chamber is shown in Figure 5. In the cross-sectional view, component 1 is the high-pressure common rail and component 2 is the 6-oriface Bosch high-pressure fuel injector. Fuel is injected into a uniformly heated, constant volume, pressure-controlled combustion chamber labeled as component 2 in the external model of the system. Component 3 is the pressure sensor used to measure the increase in pressure due to combustion, chamber cooling due to fuel injection, and oscillations after peak pressure. Fuel line pressure is measured as well using component 4 in the diagram in Figure 5.

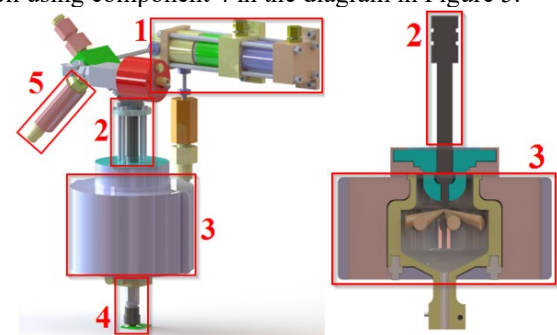


Figure 5: Instrumentation and CAD Model of the PAC CID 510 Constant Volume Combustion Chamber

The authors conducted 5 conditioning cycles of injection, combustion, and exhaust before taking measurements for 15 combustion cycles. Pressure data from each of the cycles is averaged for the 15 cycles to provide an accurate bank of data. These testing cycles follow the ASTM standard D7667-14.a represented in Table 5.

Table 5: ASTM Standards used in the CVCC Experimentation (ASTM D7668-14.a)

		• · · · · · · · · · · · · · · · · · · ·		
Wall Temp.	Fuel Injection Pressure	Coolant Temp.	Injection Pulse Width	Chamber Pressure
		- т		
595.5 °C	1000 bar	50 °C	2.5 ms	20 bar

For each researched fuel, the averaged pressure data from the 15 combustion cycles was plotted against time as shown in Figures 6 and 7 allowing for determination of the average ID and CD for each fuel. Figure 6 contains the pressure traces for ULSD and the blends with S8 and Figure 7 shows the pressure traces for ULSD and the blends with IPK. This was done to iterate the various researched fuels and fuel blends more clearly as the pressure trace for IPK is so much more extended than that of S8 and ULSD.

The ID is defined as the time from SOI (0 ms) until LTHR is observed to peak. The CD is considered to be the time from SOI to the peak of HTHR or midpoint of the pressure curve [23]. Equation 4 is used to determine the DCN from the ignition delay and combustion delay [24,25]. These results are tabulated in Table 6.

Table 6: ID, CD and DCN of All Researched Fuels

	ID	CD	DCN
S8	2.74	3.90	62.2
30USLD70S8	2.89	4.15	57.65
50ULSD50S8	2.98	4.28	55.71
ULSD	3.56	5.15	47
50ULSD50IPK	3.46	6.22	41.15
30ULSD70IPK	3.87	8.017	36.01
IPK	5.30	17.17	25.88

With respect to ignition delay, neat S8 was observed to have the shortest ID at just 2.74 ms, while IPK had a considerably longer ID at 5.30 ms. The ID of ULSD was measured as 3.56 ms. The combustion delay of the fuels exhibited a significant contrast between S8 with a CD of 3.90 ms, ULSD at 5.1523 ms, and IPK far behind at 17.17 ms.

There is an exponential correlation between increasing CD with increasing mass concentration of IPK compared with neat ULSD. This is confirmed in the pressure trace as IPK has a significantly slower combustion event with a lower pressure rise rate.

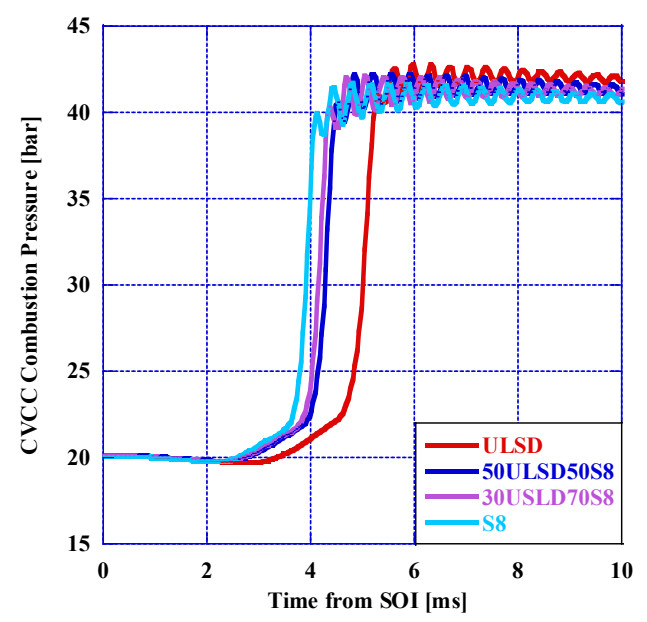


Figure 6: Pressure Curve for Neat ULSD, Neat S8 and the Blends of ULSD and S8 in CVCC

From an analysis of the chemical composition of each of the researched fuels as seen in Table 1, it can be determined that there is a correlation between the percentage of normal paraffins and the DCN, ID, and CD of the fuel. As the ratio between normal paraffins and iso paraffins increases, the DCN of the fuel increases as the straight chain hydrocarbons which constitute n-paraffins have single bonds which break more readily than the double bonds found in iso-paraffins. For each of the measurements, the DCN was calculated using the durations of the ignition delay and combustion delay using the relationship outlines in Equation 4.

$$DCN = 13.028 + \left(-\frac{5.3378}{ID}\right) + \left(\frac{300.18}{CD}\right) + \left(-\frac{12567.90}{CD^2}\right) + \left(\frac{3415.32}{CD^3}\right)$$

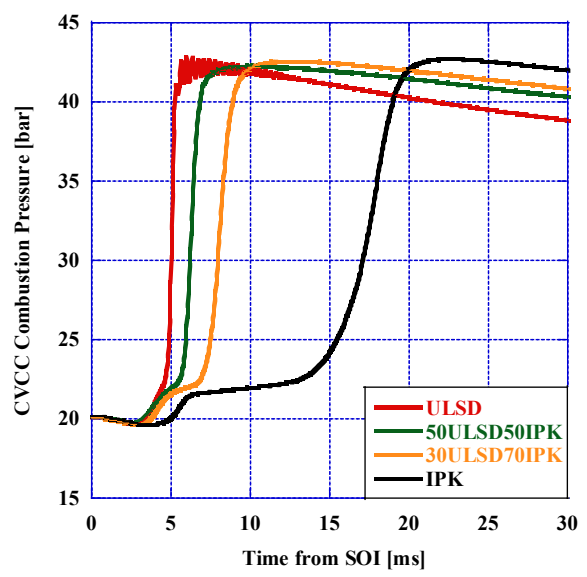


Figure 7: Pressure Curve for Neat ULSD, Neat IPK and the Blends of ULSD and IPK in CVCC

Also observed in the pressure traces from the CVCC are the ringing events occurring around the peak combustion pressure. To better analyze this, a zoomed scale on the pressure axis at the peak is employed in Figures 8 and 9. Additionally, for Figure 9, due to the long CD of IPK, the x-axis is shown on a logarithmic scale.

When comparing ULSD to S8 and S8 blends (Fig. 8), ringing is present for all fuels, however neat S8 exhibited the most ringing due to the increased DCN and reduced ID and CD. Both S8 blended fuels exhibited ringing events closer in magnitude and frequency to that of neat S8 than neat ULSD, due to the significant increase in DCN with the addition of S8.

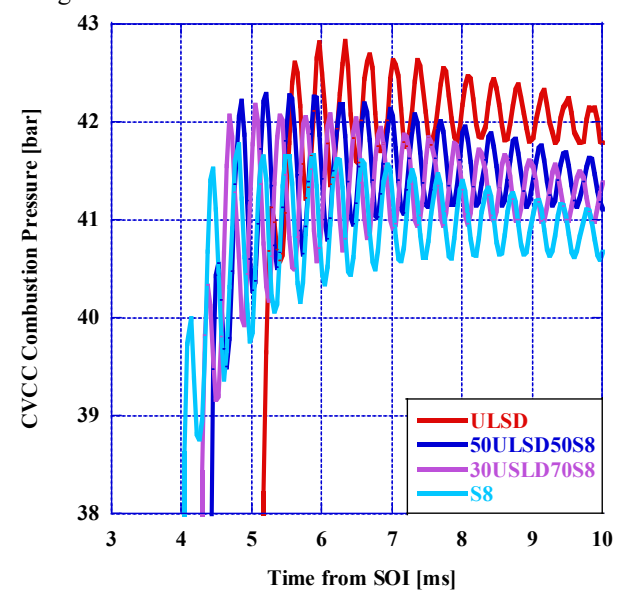


Figure 8: Combustion Instabilities and Pressure
Oscillations for Neat ULSD, Neat S8 and the Blends of
ULSD and S8 in CVCC

When comparing ULSD to IPK and IPK fuel blends (Fig. 9), ringing events of any significant magnitude are only noted for ULSD, vanishing nearly completely with the addition of IPK in the 50% mass blend. This is due to the long ID and CD of IPK, resulting in a lower DCN which is less favorable for ringing. The x-axis in Figure 9 is logarithmic in order to show all peak pressures for neat ULSD, neat IPK, and the ULSD/IPK blends.

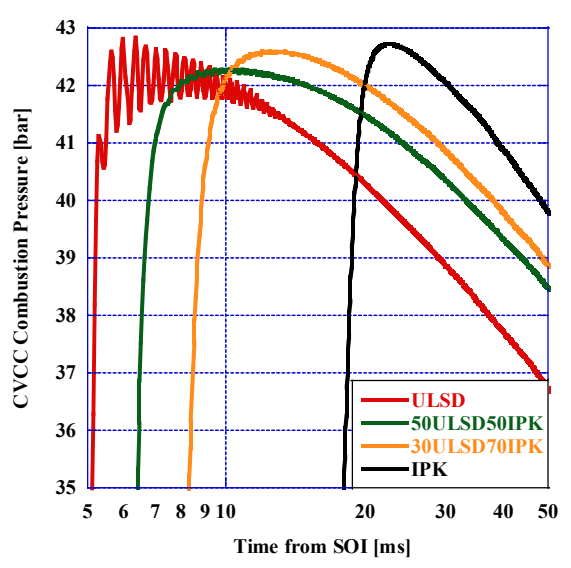


Figure 9: Peak Pressures on a Logarithmic Scale for Neat ULSD, Neat IPK and the Blends of ULSD and IPK in CVCC

The time after SOI that the fuel reached its peak pressure is related to the pressure rise rate of the fuel—the steepness of the pressure trace after the ignition delay. The peak pressure of IPK (42.73 bar) was observed to be higher than that for S8 (41.77 bar), but the time at which the peak occurred was also the longest (22.72 ms for IPK, compared with just 4.8 ms for S8). This correlates with the ignition delays for these fuels, with S8's shorter ID and high DCN causing pressure to peak earlier than IPK with its low DCN and extended ID. The greatest peak pressure was observed with ULSD at 42.84 bar, at a time of 6.32 ms. All peak pressures for all researched fuels are listed in Table 7.

Table 7: CVCC Peak Pressures and Time at Peak for Each of the Researched Fuels

Researched Fuel	Time (ms)	Peak Pressure (bar)
S8	4.8	41.77
30ULSD70S8	5.04	42.19
50USLD50S8	5.2	42.29
ULSD	6.32	42.84
50ULSD50IPK	9.4	42.29
30ULSD70IPK	12.32	42.6
IPK	22.72	42.73

The Apparent Heat Release Rate (AHRR) was calculated from the pressure trace and is useful to identify the combustion regions of LTHR, NTCR, and HTHR. The AHRR quantifies the useable energy produced by the fuel's combustion,

or the amount of energy inside the combustion chamber available to increase the surrounding temperature during the combustion event. The equation used to calculate AHRR comes from the first law of thermodynamics (Eq. 5).

$$\frac{dQ}{dt} = \frac{1}{\gamma - 1} V \frac{dP}{dt} \tag{5}$$

After SOI, the AHRR becomes negative due to the vaporization of the fuel which absorbs heat inside the combustion chamber, causing a drop in temperature (reflected as the negative trend in AHRR) and pressure (Figs. 6-7, 10-11). The LTHR region begins when the AHRR becomes positive, correlating with cool flame formation and ends when the rising HTHR value matches the peak LTHR value [25]. In between the peak LTHR value and the conclusion of LTHR is the NTCR, where the slope of the AHRR curve is negative due to the formation of peroxides (in particular, ketohydroperoxides), which require more energy to form than is released from the combustion of the fuel [27,28]. When HTHR peaks (around the midpoint of the pressure curve), the CD is said to conclude. The end of combustion (EOC) is defined at the first AHRR crossing of zero after peak HTHR. Subsequent fluctuations in AHRR after EOC are considered ringing.

The AHRR plot for ULSD, S8, and S8 blends is provided below (Fig. 10). Neat S8 was observed to have the shortest CD and largest peak in AHRR. Additionally, neat S8 and S8 blends took less time in LTHR. All fuels exhibited ringing after EOC, with neat S8 and the blends exhibiting more significant ringing events.

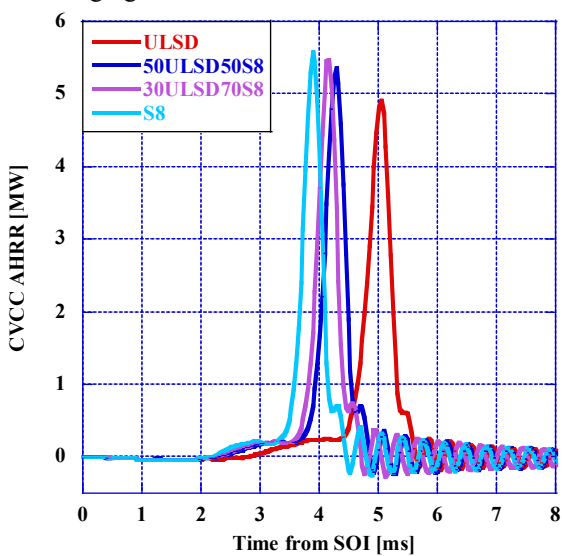


Figure 10: Apparent Heat Release Rate for Neat ULSD, Neat S8 and the Blends of ULSD and S8 CVCC

The AHRR plot for ULSD, IPK, and IPK blends is provided below (Fig. 10). Neat ULSD was observed to have the shortest CD and a significantly higher peak in AHRR compared to neat IPK and IPK blends. Additionally, IPK and IPK blends spent much more time in LTHR than ULSD. No significant ringing events were observed after EOC for IPK and IPK blends.

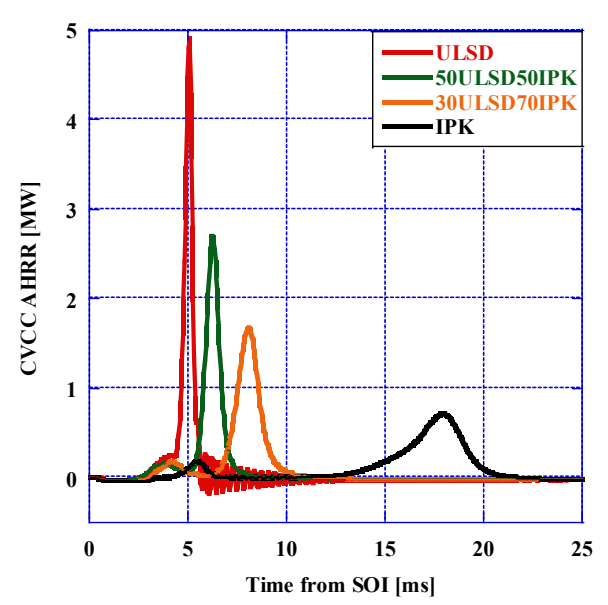


Figure 11: Apparent Heat Release Rate for Neat ULSD, Neat S8 and the Blends of ULSD and S8 in CVCC

Closer analysis of the LTHR of ULSD, S8, and S8 blends (Fig. 12) reveals the decreased size of the LTHR region for S8, as well as the shorter time to vaporize (2.18 ms for S8 compared with 2.7 ms for ULSD).

As the DCN of the research fuel increased, the slope of the cool flame formation region during LTHR increased. Although neat S8 has the shortest ID and CD, the NTC region is longer as a fraction of its total combustion time as well as shows a more significant reduction in AHRR than that of ULSD.

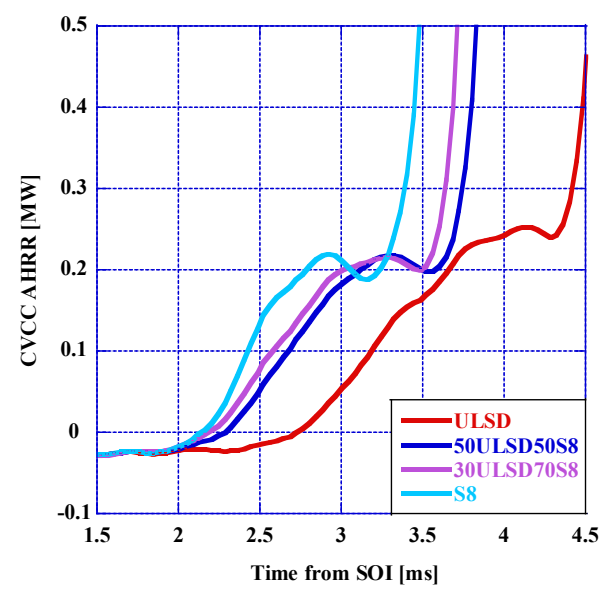


Figure 12: Low Temperature Heat Release Regions for Neat ULSD, Neat S8 and the Blends of ULSD and S8 in CVCC

Analysis of the LTHR of ULSD, IPK, and IPK blends (Fig. 13) reveals the extended LTHR of neat IPK and IPK blends, resulting in a longer period of cool flame formation which

increases the stability of combustion and reduction in ringing as seen in the pressure traces.

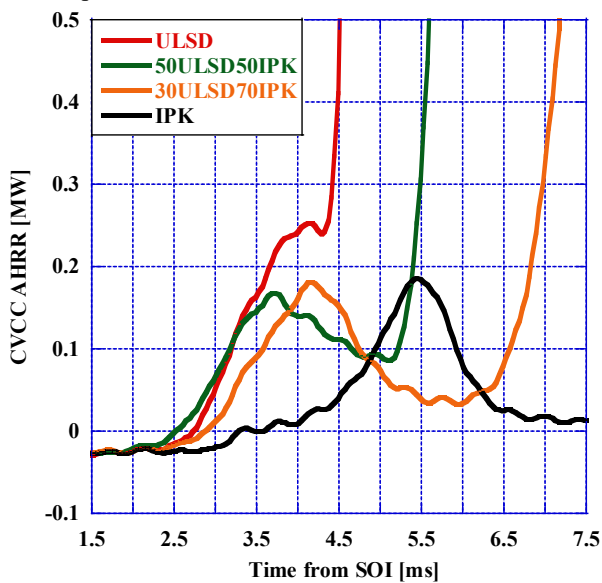


Figure 13: Low Temperature Heat Release Regions for Neat ULSD, Neat IPK and the Blends of ULSD and IPK in CVCC

The energy released in each combustion region, as well as the total energy released for each researched fuel is presented in Table 8. Neat S8 released the least amount of total energy at 2450.2 J, with 93% of its energy released during HTHR; while LTHR constituted only 7% of the total energy released. The greatest amount of energy released occurred with neat IPK releasing 2728.2 J, of which 19.6% (535.03 J) occurred in LTHR—the highest percentage of all researched fuels. Neat IPK also released the greatest fraction of energy in NTCR of all researched fuels at 411.91 J (15.1%). ULSD's total energy release of 2650.2 J was in between neat S8 and neat IPK, with 11.3% occurring in LTHR region, and 3.3% in NTCR.

Table 8: Energy Released for Each Combustion Region and Total Energy Released for All Researched Fuels in CVCC

Total Ellergy Released for All Researched Liders in CVCC				
	LTHR [J] /	NTCR [J] /	HTHR [J] /	Total
	% of total	% of total	% of total	[J]
S8	171.93 / 7	72.9 / 3	2278.29 / 93	2450.2
30USLD70S8	199.95 / 8	58.28 / 2.3	2301.74 / 92	2501.6
50ULSD50S8	182.29 / 7.4	58.55 / 2.4	2272.18 /	2454.4
			92.6	
USLD	300.11 / 11.3	87.47 / 3.3	2350.09 /	2650.2
			88.7	
50ULSD50IPK	294.61 /	187.46 / 7.1	2361.03 /	2655.6
	11.1		88.9	
30ULSD70IPK	432.85 / 16	270.72 / 10	2270.48 / 84	2703.3
IPK	535.03 /	411.91 /	2193.2 / 80.4	2728.2
	19.6	15.1		

COMBUSTION ANALYSIS IN THE IDI RESEARCH ENGINE

Engine experimentation was conducted in a high compression ratio Indirect Injection (IDI) single-cylinder research engine. Each of the 5 research fuels, (ULSD, 30ULSD70S8, 50ULSD50S8, 30ULSD70IPK, and

50ULSD50IPK) were ran in the engine at 5, 6, and 7 bar IMEP at 2400 rpm at peak effective torque. A complete diagram of the engine instrumentation can be found in Figure 14. The engine is liquid cooled and mounted on a hydraulic dynamometer. All crank angle measurements and TDC determinations were measured using an OMRON E6C2 optical rotary encoder with 2000 pulses per revolution. All parameters listed in Table 9 remained constant for all experimentation.

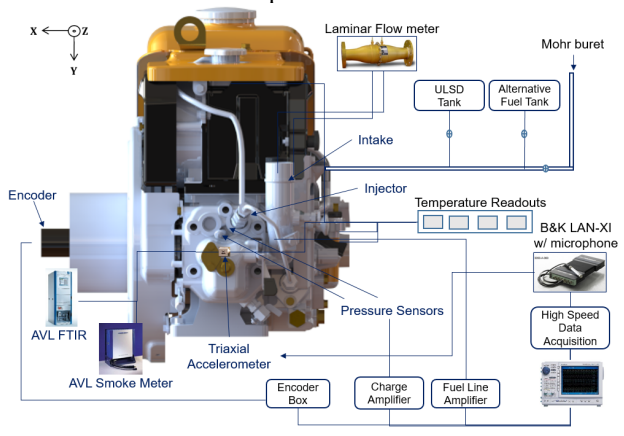


Figure 14: Instrumentation Diagram for the High Compression Ratio Research Engine [29]

Table 9: Research Engine Specifications

Table 9. Research Engine Specifications		
Parameter	Value	
Emissions Regulation	Tier 4	
Displaced volume	0.35 L	
Stroke	70 mm	
Bore	77 mm	
Connecting Rod Length	111 mm	
Compression ratio	23.5:1	
Injection Nozzle	1 Orifice x 0.20 mm	
Injection Pressure (Nominal)	150 bar	
Number of Cylinders	1	
Engine Effective Power	5.2 kW@ 3000 rpm	
Engine Effective Torque	18 Nm @ 2400 rpm	

This engine was chosen for this experimentation not only for the high compression ratio, but also for the highly turbulent, triple vortex prechamber. The IDI configuration relies more on the vaporization properties of the fuel and can have in special cases better fuel economy and lower exhaust emissions than that of DI engines as reported in [30,31]. The prechamber increases fuel/air mixing and induces multi-phase combustion caused by the ejection of the flame front from the prechamber to the main chamber [32]. This in combination with the Pintauxtype hydraulically actuated injector (1x0.200mm nozzle) accentuates the thermophysical properties of the researched fuel [33]. A diagram of the prechamber can be found in Figure 15. Instrumentation for this configuration includes a Kistler type 6053 CC pressure sensor in the main chamber and a Kistler type 6056A pressure sensor in the prechamber shown in the CAD model of the head in Figure 16.

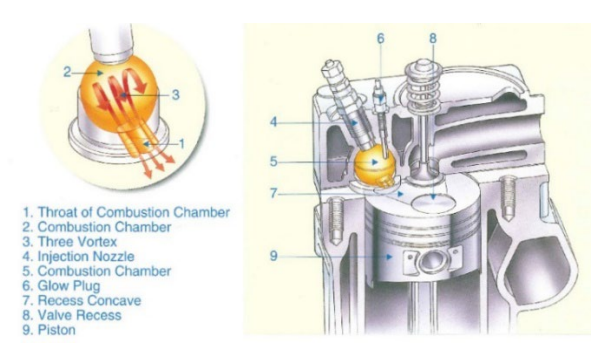


Figure 15: Illustration of the Instrumentation and Configuration of the Highly Turbulent Prechamber [34]

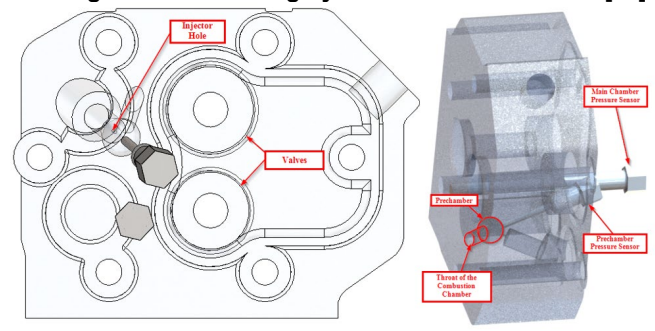


Figure 15: CAD Model of the Pressure Sensor Placement for the Main Chamber and the Prechamber on the Head

Each of the fuels was run at three loads while all other parameters remained constant. Figures 16-28 display the graphs which represent the combustion characteristics for all researched fuels at 7 bar IMEP. The graph in Figure 16 shows both the combustion pressure in the main chamber and the fuel line pressure with the motoring curve obtained in the main combustion chamber for reference. As both S8 and IPK have a lower density and viscosity than that of ULSD, the fuel pressure that can be built in the lines before adequate injection can take place is lower for each of the blends when compared to ULSD.

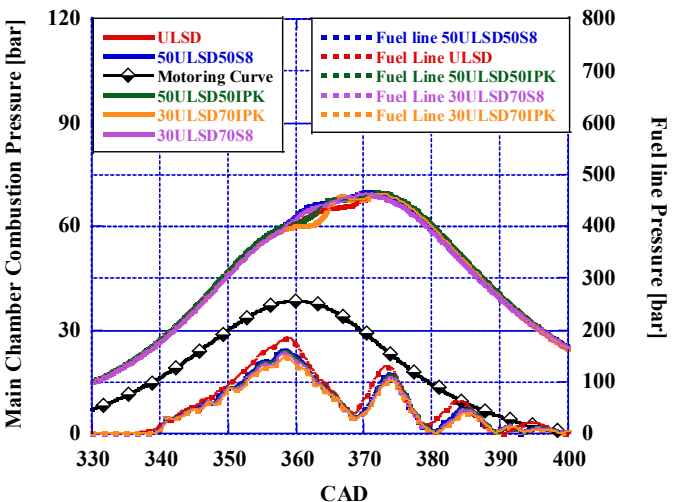


Figure 16: MC Pressure and Fuel Line Pressure for ULSD and the F-T Blends in Engine

In Figure 17, the fuel line pressure is presented for each of the researched fuels. Due to the lower viscosity of the F-T

fuels, the blends which contain F-T fuel do not build as much pressure in the fuel lines when compared to ULSD. As the hydraulically actuated Pintaux injector begins to open under rising fuel line pressure, the lower density and viscosity of the F-T fuel blends allows enough fuel to pass through the injector for combustion to take place and maintain the IMEP. Therefore, peak fuel line pressures for the F-T fuel blends are lower than for ULSD. As IPK has the lowest viscosity of each of the neat fuels, the 30ULSD70IPK blend achieved the lowest peak fuel line pressure at 147.63 compared to ULSD at 184.12. The rest of the peak fuel line pressures and the CAD for which they occur are listed in Table 10.

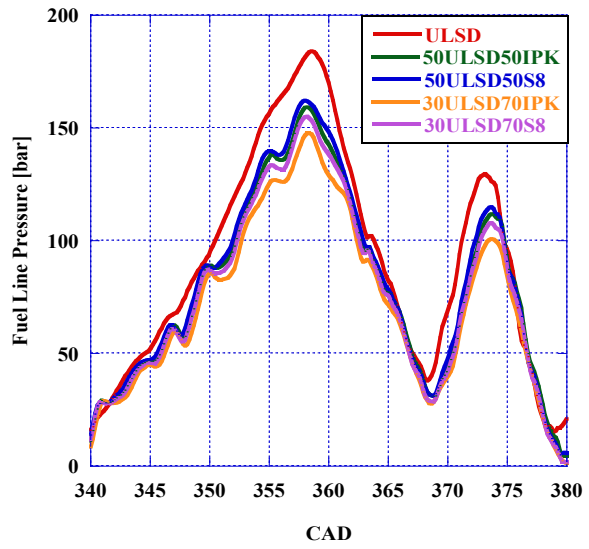


Figure 17: Zoom of the Fuel Line Pressure for ULSD and the F-T Blends in Engine

Table 10: Peak Fuel Line Pressure for Each of the Researched Fuels

Researched Fuel	Peak Fuel Pressure [bar]/CAD	% Difference to ULSD
30ULSD70S8	155.15 / 358.2	-15.73/-0.1004
50ULSD50S8	162.26 / 358.02	-11.87/-0.1506
ULSD	184.12 / 358.56	N/A
50USLD50IPK	159.15 / 358.2	-13.56/-0.1004
30ULSD70IPK	147.63 / 358.38	-19.82/-0.0502

Following the analysis of the fuel line pressure, the combustion pressure in both the prechamber and the main chamber are compared to one another to determine the effect of changing DCN on the dual-chamber configuration.

The graph in Figure 18 shows the pressure trace for the main chamber zoomed to better understand the phenomena around peak pressure and combustion phasing. The fuel blends which contain a higher percentage of IPK, with reduced DCN, have a delay in ignition and the combustion pressure rise when compared to neat ULSD consistent with previous findings on the combustion characteristics of neat IPK [10]. The blends with a higher DCN, (those containing S8), however, see little to no delay in combustion and exhibit a much smoother combustion pressure curve when compared to USLD and the IPK blends.

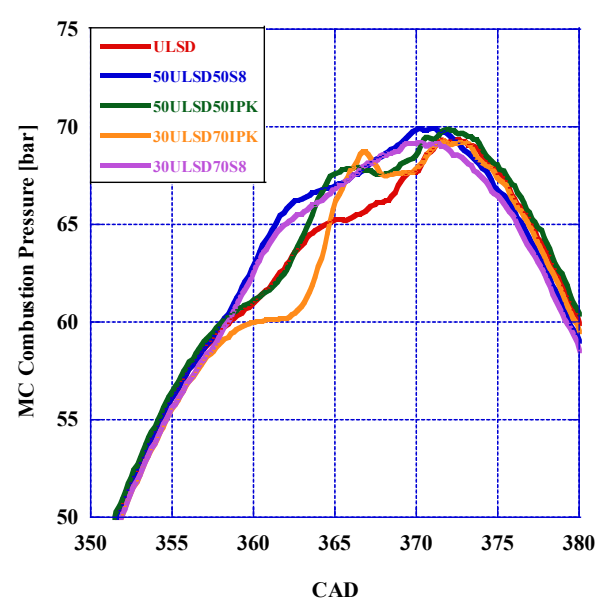


Figure 18: Zoom of Peak In-Cylinder Pressure in the Main Chamber for ULSD and the F-T Blends in Engine

Figure 19 is the zoom of the pressure trace for the pressure measured in the prechamber. For each of the researched fuels, turbulence and pressure oscillations can be seen in prechamber which are not present in the main chamber. This is due to the swirl pattern in the prechamber causing regular pressure pulses as the pressure sensor is buffeted by the in-chamber swirl. The blends with S8 begin combustion sooner showing very little drop in pressure after TDC as combustion propagates into the main chamber. Following the trend in Figure 18, blends with IPK show a delay in combustion and a more significant drop in pressure as combustion propagates between the two chambers.

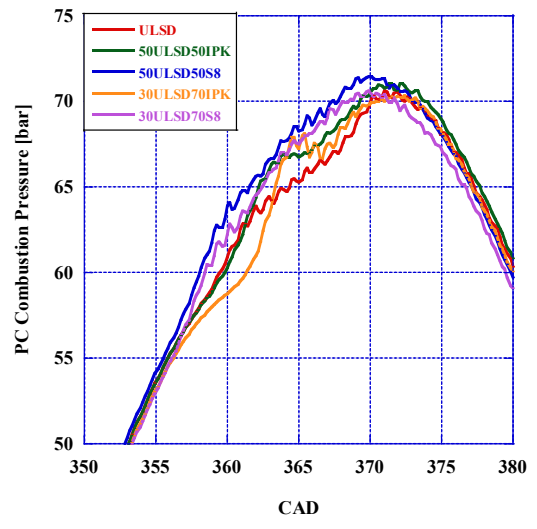


Figure 19: Zoom of the Peak In-Cylinder Pressure in the Prechamber for ULSD and the F-T Blends in Engine

To further analyze the relationship between the two chambers and the effect of DCN on combustion, a difference was taken between the pressure in the prechamber and the pressure in the main chamber for each fuel. The resulting graph is shown in Figure 20. The S8 blends with a higher DCN show a greater similarity in the pressures in the prechamber and main chamber.

As DCN is decreased with the addition of IPK, there can be seen a greater pressure difference between the two chambers. S8's affinity for autoignition as reflected in the DCN causes more points of ignition and homogeneous combustion as the fuel is less affected by areas of lower pressure or lower temperature. The 50% and 70% IPK blends exhibit results consistent with the findings from previous investigations [10] due to the increase in physical ID and chemical ID. An unequal distribution of temperatures and pressures causes only some areas of the combustion chambers to ignite the fuel of a lower DCN. The areas which do not ignite continue to vaporize the fuel creating a quasi-homogeneous air-fuel ratio and more ideal conditions for rapid flame propagation.

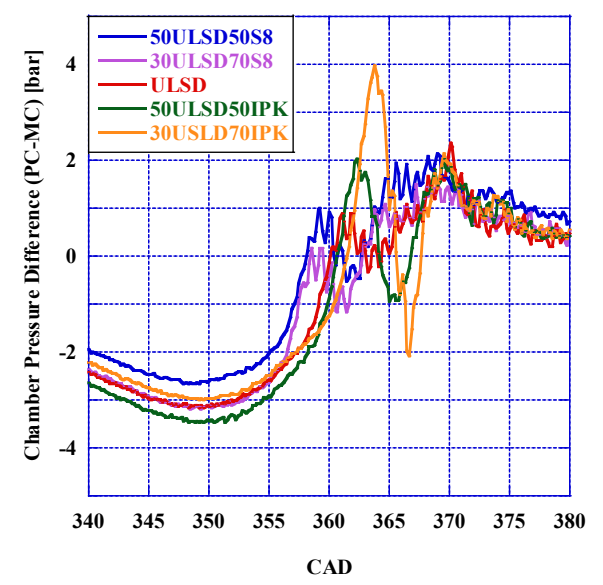


Figure 20: Pressure Difference between the Prechamber and the Main Chamber in Engine

An analysis of the Apparent Heat Release Rate (AHRR) in both the main chamber and the prechamber was conducted using Equation 6 and the results are displayed in Figures 21 and 22, respectively.

$$\frac{dQ}{d\theta} = \frac{1}{(\gamma - 1)} V \frac{dP}{d\theta} + \frac{\gamma}{(\gamma - 1)} P \frac{dV}{d\theta}$$
 (6)

In both chambers there can be seen the two-phase combustion. This is observed, in Figure 21, as an initial pulse in AHRR followed by a much larger pulse in AHRR which represents the main combustion process.

This two-phase combustion was found to be more prominent as the DCN of the researched fuel decreases with the 30ULSD70IPK blend showing both the largest initial pulse in AHRR and the largest drop in AHRR between the combustion phases. In previous investigations with neat IPK, the two-stage combustion phases of AHRR occur closer together with the increase in mass percent blends of IPK due to the autoignition resistance [10].

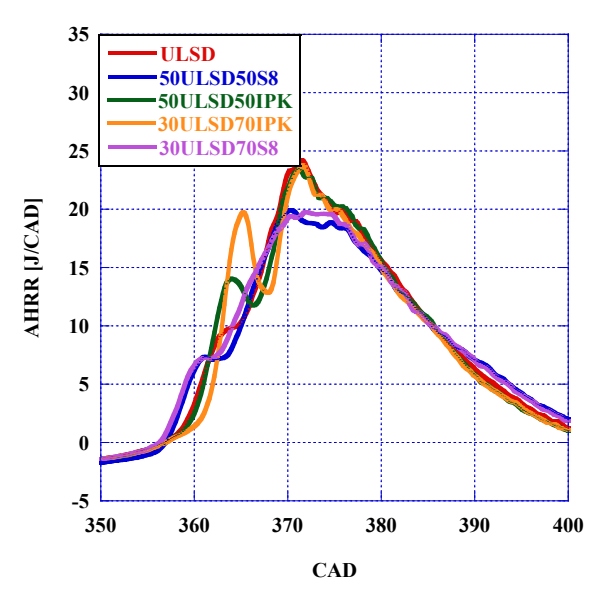


Figure 21: AHRR in the Main Chamber for ULSD and the F-T Blends in Engine

The graph in Figure 22 shows the AHRR as derived from the pressure in the prechamber. Since fuel is injected into the prechamber, the AHRR in the prechamber precedes the AHRR in the main chamber with the initial spike in AHRR happening much closer to TDC in the prechamber. Additionally, as the AHRR in the prechamber decreases, the AHRR in the main chamber increases representing the flames' propagation from the prechamber to the main chamber. Following the trend in Figure 21, the two-phases of the AHRR are more prominent as the DCN of the researched fuel decreases. In both Figures 21 and 22, the blends with S8 show an earlier increase in AHRR due to the increase in DCN.

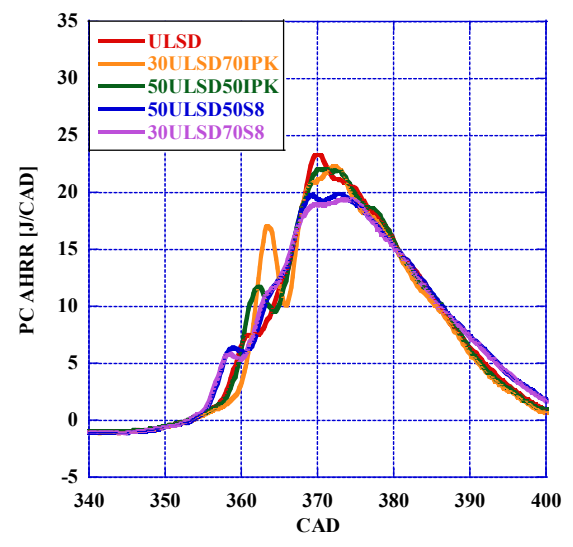


Figure 22: AHRR in the Prechamber for USLD and the F-T Blends in Engine

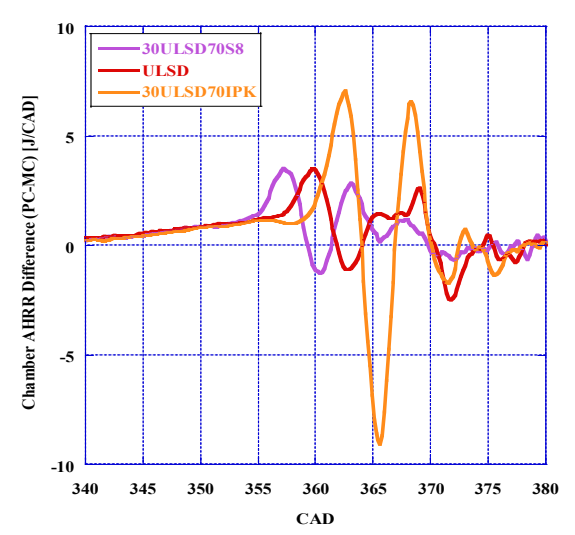


Figure 23: Difference in AHRR between the Prechamber and the Main Chamber for USLD and the F-T Blends in Engine

Similar to the pressure analysis, a difference was taken between the prechamber and the main chamber for the AHRR with the resulting graph shown in Figure 23. For clarity, only the fuel blends with 70% by mass F-T fuel are shown with ULSD as a reference. In this graph, positive values represent larger AHRR values in the prechamber and negative values represent larger AHRR values in the main chamber. Here the dual-phase combustion process is exemplified for each of the researched fuels with an initial increase in the prechamber followed by a drop in the values associated with greater heat release in the main chamber. ULSD has the smallest magnitude of oscillations between the prechamber and the main chamber. This is due to the lower vaporization rate of ULSD when compared to the synthetic aerospace fuels slowing the oscillation of the flame front between the two chambers.

An analysis of the Pressure Rise Rate (PRR) was conducted and the resulting graph of the PRR is shown in Tables 11 and 12. The PPRR values for the researched fuels are provided in Table 11, and Table 12 shows the point at which PRR changes inflection from decreasing to increasing after TDC as determined by the second derivative of pressure. This is an indication of the start of combustion as the exothermic reactions start to have a net positive influence on chamber pressure. Following the trends in Figures 18-23, the blends with S8 begin to increase in PRR before TDC at 357° CAD. Conversely, the blends with IPK do not increase in pressure until after TDC, and also show the largest Peak Pressure Rise Rate (PPRR).

Table 11: Peak Pressure Rise Rate during Combustion for Each of the Researched Fuels

Researched Fuel	Peak Pressure Rise Rate [bar/CAD]	% Difference from ULSD
30ULSD70S8	1.73	+35.15
50ULSD50S8	1.73	+35.15
ULSD	1.28	N/A
50USLD50IPK	1.95	+52.34
30ULSD70IPK	3.28	+156.25

Table 12: Change in Infection of Pressure Rise Rate due to Combustion

Researched Fuel	Pressure Rise Rate Inflection Point [CAD]	% Difference from ULSD
30ULSD70S8	356.76	-0.60
50ULSD50S8	356.94	-0.55
ULSD	358.92	N/A
50USLD50IPK	359.82	+0.25
30ULSD70IPK	361.08	+0.60

The heat flux results are displayed in Figures 25 and 26 where Figure 25 shows the heat flux for ULSD and the blends with S8 and Figure 26 shows the heat flux for ULSD and the blends with IPK. Heat flux was calculated using in-cylinder Reynold's number, air viscosity, and air thermal conductivity calculated using Equations 7, 8, and 9 [35].

$$Re(\alpha) = \rho(\alpha) \frac{S * N * D}{30 * \mu(\alpha)}$$
 (7)

$$\mu(\alpha) = 4.94 \left(\frac{1273.15 + 110.4}{T_A + 110.4} \right) *$$

$$* \left(\frac{T_A(\alpha)}{1273.5} \right)^{1.5} * 10^{-5}$$
(8)

$$\lambda_A(\alpha) = -1.2775 * 10^{-8} * T_A(\alpha)^2 + +7.66696 * 10^{-5} * T_A(\alpha) + 0.0044488$$
(9)

These values determined for the instantaneous volume averaged gas properties were then used to determine the heat flux in a thermodynamic model developed by Borman-Nishiwaki [35]. The model was then refined by Soloiu et. al. for use in determining the convection and radiation heat fluxes using Equation 10 [36].

$$\dot{q}(\alpha) = Ct * \frac{\lambda_A(\alpha)}{D} Re(\alpha)^{0.7} \left(T_{A(\alpha)} - T_W \right) + \sigma * \varepsilon (T_A^4(\alpha) - T_W^4) * A$$
(10)

The results of the heat flux analysis are displayed in Figures 25 and 26 where Figure 25 shows the heat fluxes for the S8 blends and Figure 26 shows the heat fluxes for the IPK blends. In can be seen in Figure 25 that with the addition of S8 there is a 5.8% reduction in the total heat flux primarily due to the 7.7% reduction in radiation heat flux.

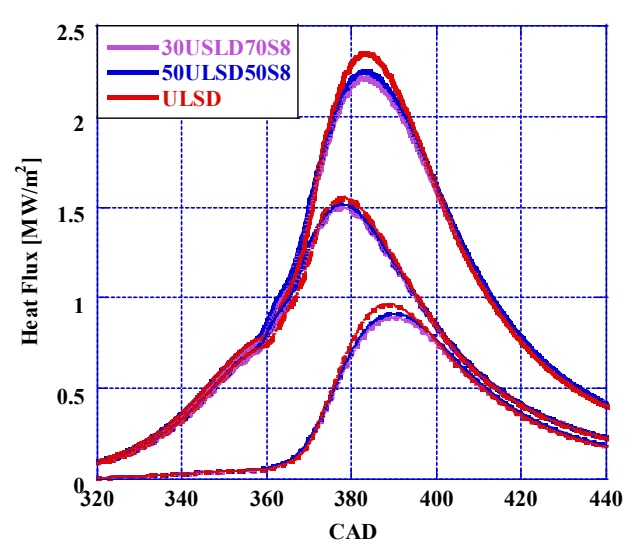


Figure 24: Heat Flux at 7 bar IMEP (Solid Line – Total Heat Flux, Dashed Line – Convection Heat Flux, Dotted Line – Radiation Heat Flux) for S8 blends with ULSD in Engine

For the IPK blends with ULSD, the heat fluxes are shown in Figure 26. For the 50ULSD50IPK blend, there is negligible change in the heat flux when compared to ULSD. With the increase in mass percentage of IPK in the blend, the total heat flux and radiation heat flux reduced by 2.55% and 4.75% respectively. Additionally, thermal and mechanical efficiencies for each of the researched fuels at 7 bar IMEP are shown in Table 13.

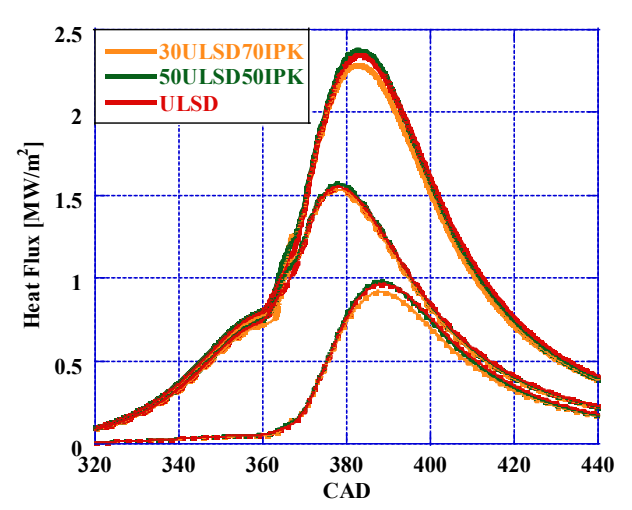


Figure 25: Heat Flux at 7 bar IMEP (Solid Line – Total Heat Flux, Dashed Line – Convection Heat Flux, Dotted Line – Radiation Heat Flux) for IPK blends with ULSD in Engine

Table 13: Thermal and Mechanical Efficiencies for each of the Researched Fuels and % Difference to ULSD

the Researched rules and // Difference to OLOD					
	Thermal	Mechanical	%diff from	%diff from	
	Efficiency	Efficiency	ULSD (ME)	ULSD (TE)	
30ULSD70IPK	43.50	40.97	1.93	-1.90	
50ULSD50IPK	43.61	40.42	0.54	-1.64	
ULSD	44.34	40.20	N/A	N/A	
50ULSD50S8	45.75	40.15	-0.12	3.18	
30ULSD70S8	45.13	40.33	0.33	1.78	

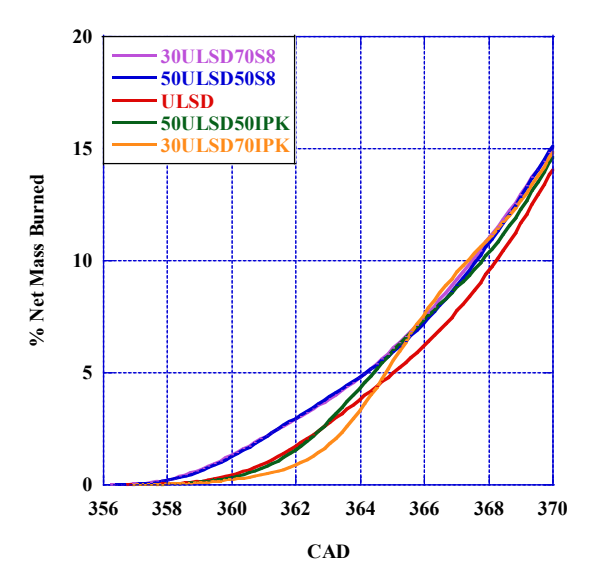


Figure 26: Zoom of the Net Mass Fraction Burned in Engine

The % mass burned as it contributes to combustion was calculated from net heat release. To illustrate the CA5 point, a zoom of the beginning of mass burned is shown in Figure 26. This integration is taken from the moment net heat release crosses zero and becomes positive for the first time to the moment that it crosses zero again and becomes negative. The % net mass burned does not reach 100% due to the heat losses due to radiation, convection, crevices, and emissions.

This analysis is used to determine the Ignition Delay (ID) as ID is defined as the difference in crank angle between the Start of Injection (SOI) and the point at which 5% of the injected fuel mass is burned as derived from the net heat release (denoted as CA5). Furthermore, combustion duration is defined as the time it takes to go from 10% mass burned, CA10, to 90% mass burned, CA90.

The S8 blends are functionally similar as they are represented in this graph and begin to burn the fuel mass before the other researched fuels at 358° CAD. The blends with IPK, though the combustion is delayed, show a more rapid increase in mass burned causing them to reach CA5 sooner than ULSD and CA10 sooner than both ULSD and the S8 blends.

Emissions Analysis

A study was conducted on the emissions produced by each of the researched fuels at 5, 6, and 7 bar IMEP to validate the viability of alternative fuels for use in reducing GHG emissions as well the effect of different chemical composition and DCN on the emissions produced from combustion. All gaseous emissions were analyzed using an MKS FTIR with soot measured using an AVL 415s Smoke Meter.

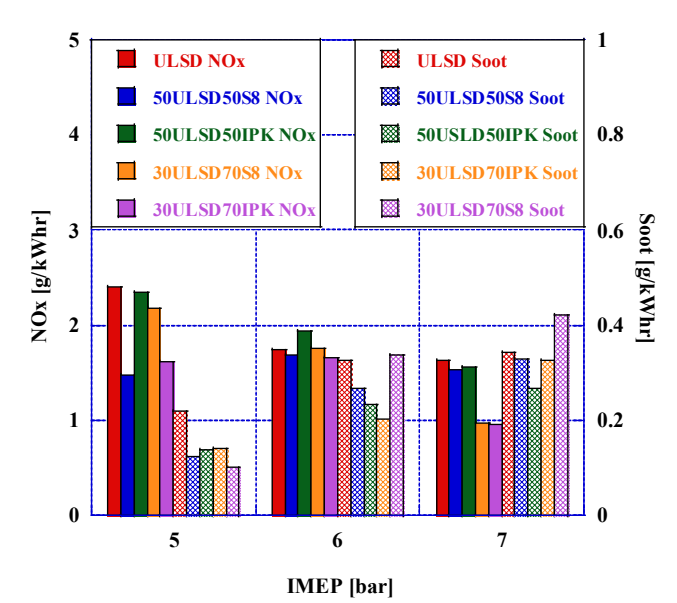


Figure 27: NO_X and Soot Emissions for ULSD and the F-T Blends at 5, 6, and 7 bar IMEP in Engine

Figure 27 is a representation of the NO_x and soot emissions for all researched fuels at all loads. It was shown that for both the IPK blends and the S8 blends there was a reduction in the NO_x emissions at all loads with the exception of 50ULSD50IPK at 6 bar IMEP.

Soot emissions for this experimentation were measured using an AVL 415s Smokemeter. For all the F-T fuel blends with the exception of the 30ULSD70S8, there was a reduction in the soot emissions at all loads due to the low aromatic content found in the synthetic fuels. Conversely, the greatest reduction in soot emissions when compared to ULSD was observed for the 30ULSD70S8 blend at 5 bar IMEP. In general, the S8 blends produced less soot at lower load while the IPK blends produced less soot at higher load.

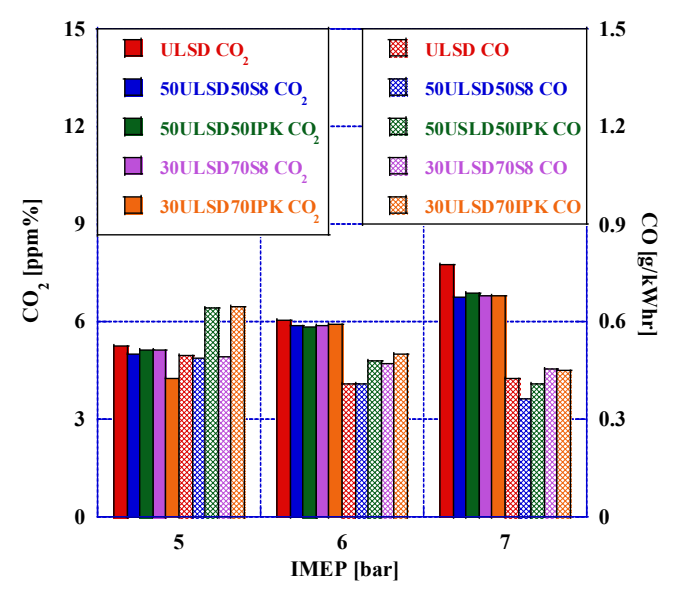


Figure 28: CO and CO₂ Emissions for ULSD and the F-T Blends at 5, 6, and 7 bar IMEP in Engine

CO and CO_2 emissions are presented in Figure 28. It was found that, for the most part, the F-T fuel blends produced more CO emissions than ULSD. At low load, the 50ULSD50IPK blend produced significantly more CO emissions than both ULSD and the S8 blends. This is an indication of incomplete combustion at lower load. Across all fuel blends at all loads there was a reduction in CO_2 emissions. All F-T fuel blends performed very similarly and produced lower CO_2 emissions at higher loads when compared to USLD.

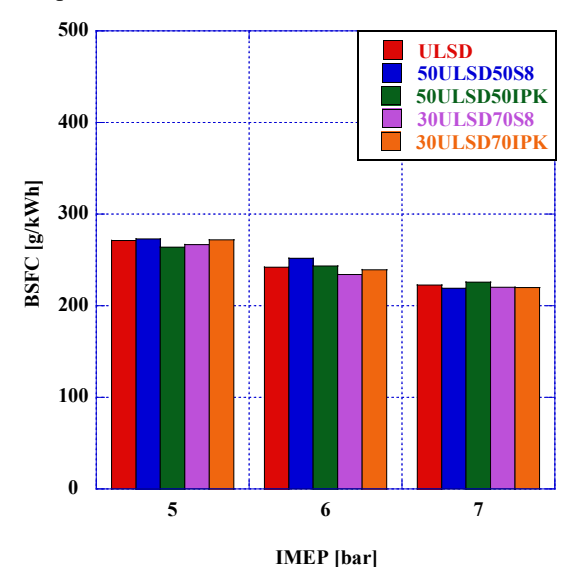


Figure 29: BSFC for ULSD and the F-T Blends at 5, 6, and 7 bar IMEP in Engine

The final analysis performed on this experimentation was a calculation of the BSFC for all fuels at all loads. These values are displayed in the graph in Figure 29. BSFC was shown to decrease as load increases for all researched fuels. The 30ULSD70S8 blend was found to perform the best for each of the researched loads followed closely by the 30USLD70IPK blend. This is due to the higher energy density in the synthetic fuels when compared to USLD. For the 50USLD50IPK blend and the 50ULSD50S8 blends, though the differences are small, the fuel consumption was found to be more effected by load. The 50ULSD50S8 blends had the lowest BSFC at 7 bar IMEP while the 50USLD50IPK blends had the lowest BSFC at 5 bar IMEP. The results of the BSFC analysis are shown in Figure 29.

CONCLUSION

A study was conducted on the thermophysical properties, combustion characteristics, and emissions output of two F-T fuels, GTL S8 (POSF5109) and CTL IPK (POSF7629) in a CVCC and a high compression ratio IDI research engine. The effects of changes in physical ignition delay and chemical ignition delay on combustion properties, combustion timing, and emissions were investigated in both neat synthetic fuels using ULSD as a reference.

An analysis of the thermophysical properties of each of the neat synthetic fuels (IPK and S8) included thermal stability and low temperature oxidation, spray atomization, mixture formation and droplet distribution, viscosity, LHV and density as an indication of the physical ignition delay for each researched fuel.

Investigations into the fundamental combustion characteristics and chemical ignition delay of the researched fuels were conducted in the CVCC for all neat fuels in addition to by mass blends of 50% and 70% of each F-T fuel blended with ULSD.

For the IDI research engine investigations, ULSD and the F-T fuel blends were run at 5, 6, and 7 bar IMEP and analyzed for both prechamber and main chamber combustion pressure, fuel consumption, fuel rail pressure, torque, and emissions at each load.

- Spray characteristics, density, viscosity, and surface tension
 were used to calculate Ohnesorge number for each of the
 researched fuels. This determination indicated that the F-T
 fuels have a higher propensity to break apart and form
 droplets when injected creating a greater surface area to
 volume ratio of the injected fuel.
- In the engine, these properties are also reflected in the lower fuel line pressures for the F-T blends from the mechanical fuel pump and injector.
- With the Ohnesorge determination and the results from the low temperature oxidation and volatility investigations, it can be determined that the neat F-T fuels have a propensity for rapid mixture formation and a short physical ignition delay when compared to ULSD.
- In the CVCC, it was revealed that the neat F-T fuels occupy the low- and high-end extremes of all the researched fuel blends for DCN and chemical ignition delay.
- It was also found in the CVCC that, as total combustion time increased with the decrease in the fuel's DCN, there was a reduction in combustion instability and ringing. Starting with the 50% by mass blend of ULSD and IPK having negligible peak pressure oscillations further decreasing with the increase in mass % of IPK in the blend and increasing with the increase in mass % of S8.
- In the fired engine, this trend was reversed with the IPK blends increasing PPRR and pressure oscillations between the two combustion chambers with an overall reduction in total combustion time while the F-T blends containing S8 saw an increase in overall combustion time and a reduction in PPRR.
- With the shorter physical ignition delay found in the thermophysical analysis for the neat F-T fuels when compared to ULSD, the F-T fuel blends experienced more rapid mixture formation when compared to USLD leading to more complete combustion as indicated by the general reduction in CO emissions for the F-T blends.
- For soot and NOx, it was found that, in general, the addition of F-T fuel to the blend reduced both emissions species.

ACKNOWLEDGEMENTS

We acknowledge the contribution of the Air Force Laboratory for suppling the experimental fuels, Christopher Mileski, Charles McGuffy, Michael Rankin, Jacques Lapeyre, from PACLP, Samuel Olesky from Kistler, and Joseph von Wolfgang from Malvern Lasers, and Coty Harrison from Yokogawa. This paper is based upon work supported by the National Science Foundation Grant No. 1950207.

REFERENCES

- [1] S. Ahmed, K. Ahmed, and M. Ismail, "Predictive analysis of CO2 emissions and the role of Environmental Technology, energy use and economic output: Evidence from emerging economies," *Air Quality, Atmosphere & Amp; Health,* vol. 13, no. 9, pp. 1035–1044, 2020.
- [2] S. Amar-Gil, A. N. Ardila-Arias, and R. Barrera-Zapata, "Obtaining and characterization of catalytic materials from waste tires for the fischer-tropsch process," *Journal of Material Cycles and Waste Management*, 2023.
- [3] Y. Jiao, R. Liu, Z. Zhang, C. Yang, G. Zhou, S. Dong, and W. Liu, "Comparison of combustion and emission characteristics of a diesel engine fueled with diesel and methanol-fischer-tropsch diesel-biodiesel-diesel blends at various altitudes," *Fuel*, vol. 243, pp. 52–59, 2019.
- [4] Y. Kidoguchi, "Effects of fuel cetane number and aromatics on combustion process and emissions of a direct-injection diesel engine," *JSAE Review*, vol. 21, no. 4, pp. 469–475, 2000.
- [5] V. Soloiu, C. J. Phillips, C. Carapia, A. Knowles, D. Grall, and R. Smith, "Exploratory Investigation of Combustion and NVH Signature of a Drone Jet Engine Fueled with IPK," AIAA Scitech 2021 Forum, 2021.
- [6] D. Luning Prak, J. Cooke, T. Dickerson, A. McDaniel, and J. Cowart, "Cetane number, derived cetane number, and Cetane Index: When correlations fail to predict combustibility," *Fuel*, vol. 289, p. 119963, 2021.
- [7] G. Labeckas, S. Slavinskas, and I. Kanapkienė, "The individual effects of cetane number, oxygen content or fuel properties on the ignition delay, combustion characteristics, and cyclic variation of a turbocharged CRDI diesel engine – part 1," *Energy Conversion and Management*, vol. 148, pp. 1003–1027, 2017.
- [8] R. Cataluña and R. da Silva, "Effect of cetane number on specific fuel consumption and particulate matter and unburned hydrocarbon emissions from Diesel Engines," *Journal of Combustion*, vol. 2012, pp. 1–6, 2012.
- [9] P. Ghosh and S. B. Jaffe, "Detailed composition-based model for predicting the cetane number of diesel fuels," *Industrial & Engineering Chemistry Research*, vol. 45, no. 1, pp. 346–351, 2005.
- [10] V. Soloiu et al., "Combustion characteristics of low DCN Synthetic Aviation Fuel, IPK, in a high compression ignition indirect injection research engine," SAE Technical Paper Series, 2023. doi:10.4271/2023-01-0272

- [11] Z. Zheng, T. Badawy, N. Henein, E. Sattler, and N. Johnson, "Effect of cetane improver on autoignition characteristics of low Cetane Sasol IPK using Ignition Quality Tester (IQT)," *Volume 2: Fuels*; Numerical Simulation; Engine Design, Lubrication, and Applications, 2013.
- [12] D. Kim, J. Martz, and A. Violi, "The relative importance of fuel oxidation chemistry and physical properties to spray ignition," *SAE International Journal of Fuels and Lubricants*, vol. 10, no. 1, pp. 10–21, 2017.
- [13] W. Jing, W. L. Roberts, and T. Fang, "Spray combustion of jet-A and diesel fuels in a constant volume combustion chamber," *Energy Conversion and Management*, vol. 89, pp. 525–540, 2015.
- [14] W. Zeng, M. Sjöberg, D. L. Reuss, and Z. Hu, "High-speed PIV, Spray, combustion luminosity, and infrared fuel-vapor imaging for probing tumble-flow-induced asymmetry of gasoline distribution in a spray-guided stratified-charge Disi engine," *Proceedings of the Combustion Institute*, vol. 36, no. 3, pp. 3459–3466, 2017.
- [15] S. Manigandan, P. Gunasekar, S. Poorchilamban, S. Nithya, J. Devipriya, and G. Vasanthkumar, "Effect of addition of hydrogen and TIO2 in gasoline engine in various exhaust gas recirculation ratio," *International Journal of Hydrogen Energy*, vol. 44, no. 21, pp. 11205–11218, 2019.
- [16] M. Tess, M. Kurman, and C.-B. Kweon, "Spray characterization and ignition delay measurements of JP-8 and IPK in a constant-pressure flow chamber," *SAE International Journal of Engines*, vol. 9, no. 2, pp. 899–909, 2016.
- [17] M. Das, M. Sarkar, A. Datta, and A. K. Santra, "Study on viscosity and surface tension properties of biodiesel-diesel blends and their effects on spray parameters for CI engines," *Fuel*, vol. 220, pp. 769–779, 2018.
- [18] G. B. Bessee, S. A. Hutzler, and G. R. Wilson, "Propulsion and power rapid response research and development (R&D) support. delivery order 0011: Analysis of Synthetic Aviation Fuels," 2011.
- [19] A. F. Alhikami, C.-E. Yao, and W.-C. Wang, "A study of the spray ignition characteristics of hydro-processed renewable diesel, petroleum diesel, and biodiesel using a constant volume combustion chamber," *Combustion and Flame*, vol. 223, pp. 55– 64, 2021.
- [20] H. Lefebvre and V. G. McDonell, *Atomization and sprays*. Boca Raton: CRC Press, 2017.
- [21] R. E. Luna and W. A. J. Klikoff, "Aerodynamic breakup of Liquid Drops.," 1967.
- [22] Kim, D., and P. Moin. "Numerical simulation of the breakup of a round liquid jet by a coaxial flow of gas with a subgrid Lagrangian breakup model." *Center for Turbulence Research, Annual Research Briefs* (2011): 15-30.
- [23] V. Soloiu, A. Weaver, L. Parker, A. Brant, R. Smith, M. Ilie, G. Molina, and C. Carapia, "Constant Volume Combustion Chamber (CVCC) investigations of Aerospace F-24 and jet-

- A in low-temperature heat release and negative temperature coefficient regions," *Energy Conversion and Management*, vol. 263, p. 115687, 2022.
- [24] da Costa RB, Coronado CJR, Hern'andez JJ, Malaquias AC, Flores LF, de Carvalho JA. "Experimental assessment of power generation using a compression ignition engine fueled by farnesane a renewable diesel from sugarcane." *Energy* 2021;233:121187.
- [25]PAC, "Cetane ID 510 Operating Manual," Petroleum Analyzer Company, 8001-00x-01E-C.
- [26] J. B. Heywood, *Internal Combustion Engine Fundamentals*. New York etc.: McGraw-Hill, 2018.
- [27] Z. Wang and S. M. Sarathy, "Third O2 addition reactions promote the low-temperature auto-ignition of N-alkanes," *Combustion and Flame*, vol. 165, pp. 364–372, 2016.
- [28] Y. Ju, C. B. Reuter, O. R. Yehia, T. I. Farouk, and S. H. Won, "Dynamics of Cool Flames," *Progress in Energy and Combustion Science*, vol. 75, p. 100787, 2019.
- [29] V. Soloiu, T. Naes, M. Muinos, S. Harp, J. Moncada, R. Gaubert, and G. Molina, "Comparison of combustion and emissions properties of jet-A vs. ULSD in both indirect and direct compression ignition engines at same IMEP," SAE Technical Paper Series, 2016-01-0733, DOI: 10.4271/2016-01-0733.
- [30] Y. KIDOGUCHI, Y. NADA, T. ICHIKAWA, H. MIYOSHI, and K. SAKAI, "Effect of pilot injection on improvement of fuel consumption and exhaust emissions of IDI diesel engines," *SAE Technical Paper Series*, 2022.
- [31] K. Iwazaki, K. Amagai, and M. Arai, "Improvement of fuel economy of an indirect injection (IDI) diesel engine with two-stage injection," *Energy*, vol. 30, no. 2-4, pp. 447–459, 2005.
- [32] J. Shin, J. Choi, J. Seo, and S. Park, "Pre-chamber combustion system for heavy-duty engines for operating dual fuel and Diesel modes," *Energy Conversion and Management*, vol. 255, p. 115365, 2022.
- [33] M. S. and R. N. Hegde, "Investigation on the performance of an IDI engine using a novel dual Swirl Combustor," *Materials Today: Proceedings*, vol. 52, pp. 1361–1367, 2022.
- [34] Animagic.com B. // S. Kempers, "Kubota engine technology," I.M.A. Kubota Technology, 2020. [Online]. Available: https://www.i-m-a.de/en/kubota_techn.html.
- [35] G. Borman and K. Nishiwaki, "Internal-combustion engine heat transfer," *Progress in Energy and Combustion Science*, vol. 13, no. 1, pp. 1–46, 1987.
- [36] V. Soloiu, J. Weaver, H. Ochieng, M. Duggan, S. Davoud, S. Harp, G. Molina, and B. Vlcek, "Cotton seed fame combustion and emissions research in a DI diesel engine," *Volume 2: Fuels; Numerical Simulation; Engine Design, Lubrication, and Applications*, 2013.

Appendix: Instrument Accuracies

Instrument	Measured Parameter	Accuracy
Brookfield DV II Pro Rotational Viscometer	Viscosity	±1.0%
Parr Constant Volume Calorimeter	Lower Heating Value	±0.3%
	Differential Thermal Analysis,	
Shimadzu DTG-60	Thermogravimetric Analysis, and Temperature	$\pm 1.0\%$
Malvern Spraytech	Sauter Mean Diameter	±1.0%
	Derived Cetane Number	±0.3%
PAC CID-510	Ignition Delay	±0.1%
1110 012 010	Combustion Dela	±0.1%
Kistler Type 6229A Transducer	Fuel Line Pressure	±0.02%
Kistler Type 6053CC	Prechamber Pressure	≤± 0.03%
Kistler Type 6056A	Main Chamber Pressure	≤± 0.03